Energy and Environmental Science, Volume 12, Issue 5, May 2019, pp. 1708-1717
DOI:10.1039/c9ee00269c

Phase-transition induced giant negative electrocaloric effect in a lead-free relaxor ferroelectric thin film

Biaolin Peng[1,2,3], Qi Zhang[2]*, Gang Bai[4], Glen J.T. Leighton[2], Christopher Shaw[2], Steven J. Milne[5], Zhipeng Gao[6], Bingsuo Zou[3], Haitao Huang[1,]*, Zhonglin Wang[7]*

[1]Department of Applied Physics, The Hong Kong Polytechnic University, Kowloon, Hong Kong SAR

[2]Department of Manufacturing and Materials, Cranfield University, Cranfield, Bedfordshire, MK43 0AL, United Kingdom

[3]Center on Nanoenergy Research, School of Physical Science & Technology, Guangxi University, Nanning 530004, China

[4]College of Electronic and Optical Engineering & College of Microelectronics, Nanjing University of Posts and Telecommunications, Nanjing 210023, China

[5] School of Chemical and Process Engineering, University of Leeds, Leeds LS2 9JT, UK

[6]School of Materials Science and Engineering, Georgia Institute of Technology, Atlanta, GA 30332-0245, USA *Correspondence to: q.zhang@cranfield.ac.uk, aphhuang@polyu.edu.hk, zhong.wang@mse.gatech.edu

Keywords: electrocaloric; thin film; sol-gel; energy storage

Abstract: Ferroelectric/antiferroelectric thin/thick films with large positive or negative electrocaloric (*EC*) effect could be very useful in designing commercial refrigeration devices. Here, a giant negative *EC* effect (maximum $\Delta T \sim -42.5$ K with $\Delta S \sim -29.3$ J K^{-1} kg^{-1}) comparable to the best positive *EC* effects reported so far is demonstrated for $0.5(Ba_{0.8}Ca_{0.2})TiO_3$-$0.5Bi(Mg_{0.5}Ti_{0.5})O_3$ (BCT-BMT) lead-free relaxor ferroelectric thin films prepared on Pt(111)/TiO_x/SiO_2/Si substrates using a sol-gel method. An electric-field induced structural phase transition (nanoscale tetragonal and orthorhombic to rhombohedral) along the out-of-plane [111] direction plays a very key role in developing the giant negative EC effect. This breakthrough will pave the way for practical applications of next-generation refrigeration devices with high cooling efficiency in one cycle by ingeniously utilizing and combining both the giant negative and positive *EC* effects. Moreover, a large energy density of 51.7 J cm^{-3} with a high power density of 1.15×10^{10} W kg^{-1} at room temperature is also achieved in the thin film, indicating that it is also an attractive multifunctional material for energy storage.

Introduction

Recently, more and more research attention has been paid to the ferroelectric/antiferroelectric (FE/AFE) thin/thick films rather than the bulk ceramic counterpart due to the higher electrocaloric (*EC*) performance.[1-3] The poor *EC* performance in bulk ceramics could be attributed mainly to their low dielectric breakdown strength (usually less than 100 $kVcm^{-1}$). The adiabatic temperature change (ΔT) or isothermal entropy change (ΔS) of a dielectric material induced by the application or withdrawal of an electric field is called the *EC* effect. The giant *EC* effect (maximum $\Delta T \sim 12$ K) obtained in the $_{PbZr0.95TiO3}$ (PZT) AFE thin film by Mischenko et al. in 2006 has evoked a wide *EC* research interest in lead-based materials in the past decade,[4-8] due to the potential commercial application in integrated circuit cooling such as computer chips.[3, 9]

So far, both normal (positive, $\Delta T > 0$) and anomalous (negative, $\Delta T < 0$) *EC* effects have been reported, which can separately exist or co-exist in one material. Particularly, it is found that the combination of both positive and negative *EC* effects in one cooling cycle would exhibit a higher efficiency in *EC* refrigeration devices than the use of a single *EC* effect. However, compared with the great progress made in positive EC effect such as $\Delta T \sim 45.3$ K in $Pb_{0.8}Ba_{0.2}ZrO_3$ AFE/FE coexistence thin film (~ 320 nm thickness) and $\Delta T \sim 53.8$ K in a $Pb_{0.97}La_{0.02}(Zr_{0.75}Sn_{0.18}Ti_{0.07})O_3$ AFE thick film (~ 2 μm thickness),[6, 7] the progress made in negative *EC* effect has still remained at a relatively low level such as $\Delta T \sim -5.76$ K in $Pb_{0.97}La_{0.02}(Zr_{0.95}Ti_{0.05})O_3$ AFE thin film (650 nm thickness),[10] $\Delta T \sim -6.62$ K in $Pb_{0.96}Eu_{0.04}ZrO_3$ AFE thin film (550 nm thickness) and $\Delta T \sim -10.8$ K in a $Hf_{0.5}Zr_{0.5}O_2$ FE thin film (9.2 nm thickness).[11, 12]

In contrast to the extensive research on the positive *EC* effect, less attention has been paid to the negative *EC* effect due to its elusive physical mechanism. Based on previous research work, the origin of the negative *EC* effective may be ascribed to some factors such as the non-collinearity between the electric field and the polarization (dipole & defect dipole).[10, 12-17] In general, the largest negative *EC* effect appears not at the largest applied electric field but at a moderate one, under which the largest degree of non-collinearity yields the maximum ΔT & ΔS.[10, 11] Therefore, increasing the possible maximum applied electric field by improving the

dielectric breakdown strength of the materials, which is normally regarded as one of effective methods to enhance the positive *EC* effect, might not be a valid method to enhance the negative *EC* effect. Chemical element doping is usually chosen to be a simple and effective method to improve the performance of materials. However, to our knowledge, the best result obtained so far in improving the ΔT of negative *EC* effect by chemical element doping is only - 6.6 K,[10, 11, 13] which is very unsatisfactory. Magneto-electric coupling was also employed to enhance the negative *EC* effect and indeed it worked at low temperatures (150 - 210 K) such as $\Delta T \sim$ - 52.2 K in the $PbZr_{0.53}TiO_{0.47}/CoFe_2O_4$ ferroelectric/ferromagnetic multilayer nanolaminate.[18] However, the negative *EC* effect degraded very sharply as the temperature increased, due to the more and more weakening magneto-electric coupling effect. Therefore, new strategies and mechanisms need to be developed to enhance the negative *EC* effect.

In this study, we report a giant negative electrocaloric (*EC*) effect (the maximum $\Delta T \sim -$ 42.5 K and $\Delta S \sim -$ 29.3 $JK^{-1}kg^{-1}$) in $0.5(Ba_{0.8}Ca_{0.2})TiO_3$-$0.5Bi(Mg_{0.5}Ti_{0.5})O_3$ (BCT-BMT) lead-free relaxor ferroelectric thin film prepared on $Pt(111)/TiO_x/SiO_2/Si(100)$ substrate by a sol-gel method. The well-designed composition is based on the $0.5BaTiO_3$-$0.5Bi(Mg_{0.5}Ti_{0.5})O_3$ prototype ceramic which behaves as an antiferroelectric but in fact is not an antiferroelectric.[19, 20] The giant negative electrocaloric effect is attributed to the electric-field induced structural phase transition (nanoscale tetragonal & orthorhombic to rhombohedral) along the [111] direction (the out-of-plane of thin film). Moreover, a large energy density with high power density at room temperature is also achieved. These breakthroughs make the lead-free thin films very attractive for practical applications as multifunctional materials.

Results and discussions

Structure

A X-ray diffraction (XRD) pattern of the BCT-BMT thin film is shown in **Figure 1(a)**. The thin film exhibits good crystallinity and almost pure perovskite phase with a strong (111) preferential orientation. A tiny amount of secondary phases (bismuth titanate or bismuth oxide) can be detected due to the excess of Bi. For the Ti-coated substrate, it is believed that a thin layer of Pt_3Ti intermediate is formed during ceramic film crystallization, which favors the (111) texture in the BCT-BMT thin film.[21] In addition to the tetragonal

ferroelectric $_{(TFE)}$ phase, the orthorhombic and the rhombohedral ferroelectric $_{(OFE}$ ^{and} $_{RFE)}$ phases can also be detected, as guided by the $_{(111)T/O/R}$ and (11-1)$_{O/R}$) in the right lower inset of **Figure 1(a)**) and the (002)$_T$, (200)$_{T/O/R}$ and (020)$_O$. The $_{TFE}$ ^{and} $_{OFE}$ phases can also be observed directly by the atom-scale high-resolution TEM (HRTEM) image, as marked by the letters T and O in **Fig. 1(b)**. With the assistance from the fast Fourier transform (FFT) spectrum, the $_{RFE}$ phase with regular hexagonal diffraction pattern (inset of **Fig. 1(b)**) was identified, as shown by the letter R. The coexistence of the T_{FE}, O_{FE} ^{and} $_{RFE}$ phases can also be further confirmed by the characteristic modes in the subsequent Raman scattering spectra. In contrast to the coexistence of the T_{FE}, O_{FE} ^{and} $_{RFE}$ phases in the thin film, only $_{TFE}$ ^{and} $_{OFE}$ phases coexist in the BCT-BMT bulk ceramic which was prepared by using solid-state reaction process, as shown in the **Figure S1**. Similar to the case of single-domain (111)-oriented $PbTiO_3$ (PT) thin films, due to the substrate effect, the phase transition changes its order from the first to second one and leads to the formation of new ferroelectric phases,[22] which do not exist in bulk PT. In particular, when the substrate imposes biaxial compression on the film prototypic state, the rhombohedral single-domain ferroelectric state is expected to form in (111)-oriented PT films,[22] especially under the induction of an applied electric field. Therefore, the appearance of the $_{RFE}$ phase in the (111)-oriented BCT-BMT thin film is also possible and reasonable.

The cross section morphology of thin film was examined by scanning electron microscopy (SEM) (the left upper inset of **Fig. 1(a)**). The film was smooth and free of micro-cracks, indicating a high quality film structure. The surface morphology of thin film was characterized by atomic force microscopy (AFM) (**Fig. 1(b)**) and SEM (**Fig. S2**). The thin film was well crystallized and nanocrystals with size of 20-50 nm were clearly visible. The gas pores formed during the decomposition of organic matter were also uniformly distributed. The surface roughness was small, and R_a and R_q were ~ 3.54 nm and ~ 4.32 nm, respectively. **Fig. 1(c)** and **Fig. S3** show the vertical ([111] direction) phase image of the piezoresponse force microscopy (PFM) of the thin film. Nanodomains with random orientation were clearly observed when the thin film was in its prepared state, as shown in **Fig. 1(c)**. Single-stripe-domain would be visible clearly in the second scanning cycle (dc bias voltage withdrew) after the first scanning cycle (dc bias voltage applied), as shown in **Fig. S3 (a),** which indicated that nanodomains with random orientation can grow up into larger FE ones under the stimulus of dc electric field.

However, the induced single-stripe-domain was extremely unstable and would fade immediately in the third scanning cycle, as shown in **Fig. S3 (b)**, indicating the relaxation behavior of the thin film. Moreover, the butterfly curves observed in the voltage-strain response, and high strain value in the inset of **Fig. 1(c)** and **Fig. S3** also indicated the piezoelectric characteristics of thin film. The result of chemical analysis by energy dispersive spectroscopy (EDS) in cross-sectional transmission electron microscopy revealed that the composition of thin film is consistent with its chemical formula, except the excess Bi and Mg which are purposely added to avoid the formation of pyrochlore phases, as shown in the inset of **Fig. S4**.

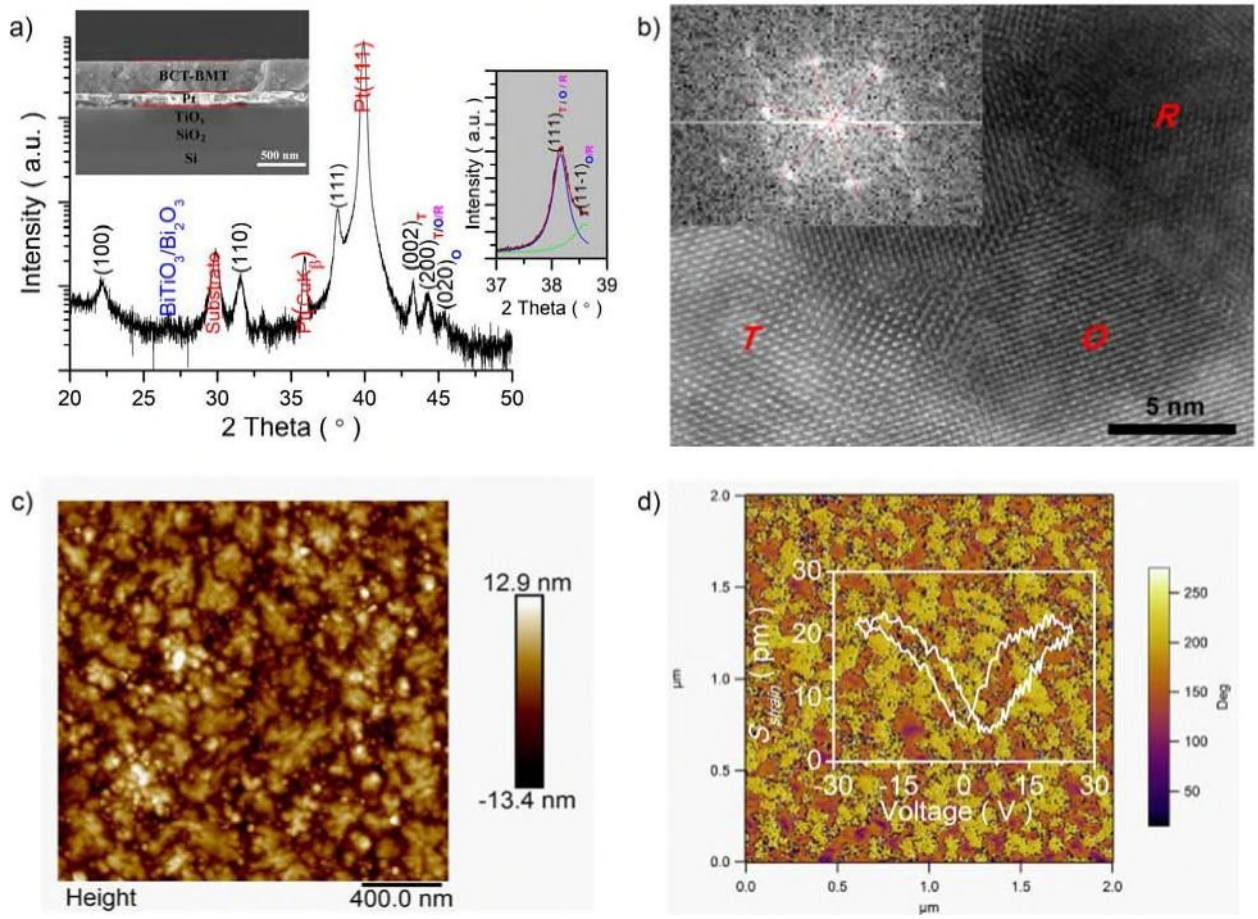

Figure 1. | 0.5(Ba$_{0.8}$Ca$_{0.2}$)TiO$_3$-0.5Bi(Mg$_{0.5}$Ti$_{0.5}$)O$_3$ (BCT-BMT) thin film. (a) XRD pattern (diffraction intensity is in a logarithmic scale). A tiny amount (less than 1%) of secondary phases ($BiTiO_3$ or Bi_2O_3) can be detected. Inset: cross-sectional SEM image. (b) Atom-scale HRTEM image. Inset: the fast Fourier transform spectrum of the *R* region. **(c)** Surface AFM micrograph. The average surface roughness of R_a and R_q is about 3.54 and 4.32 nm, respectively. **(d)** PFM vertical phase image. Inset: butterfly curve of the amplitude & voltage.

The upper part of **Figure S5(a)** shows the cross-sectional TEM image of thin film. Nanocrystals are visible clearly, and can also be identified by the discontinuous selected area electron diffraction rings as shown in the lower part**.** The upper part of **Fig. S5(b)** shows the corresponding HRTEM image of ferroelectric domains in **Fig. S5(a)**. Lamellar nanodomains with ~ 0.9 nm width which intercrossed with each other can be visible clearly. The lower part of **Fig. S5(b)** also gives the HRTEM image of the interface between the thin film and Pt bottom electrode. The smooth interface as marked by the red dotted line reveals a good growth between electrode and thin film. **Fig. 2(a) - 2(d)** and **Fig. S5(c) – S5(h)** show the evolution of lamellar nanodomains (~ 0.9 and 1.8 nm in region A and ~ 1.8 nm in region B) as the temperature increased from 20 °C to 470 °C at a step of 50 °C. The traces of most lamellar nanodomains were still visible up to 370 °C, except those domains with 1.8 nm width in region A (**Fig. 2(c)**). As the temperature increased again, all lamellar nanodomains almost disappeared, as shown in **Fig. 2(d)** (420 °C) and **Fig. S5(h)** (470 °C). For the abnormal phenomenon, detailed discussion will be carried out in the subsequent parts of this article.

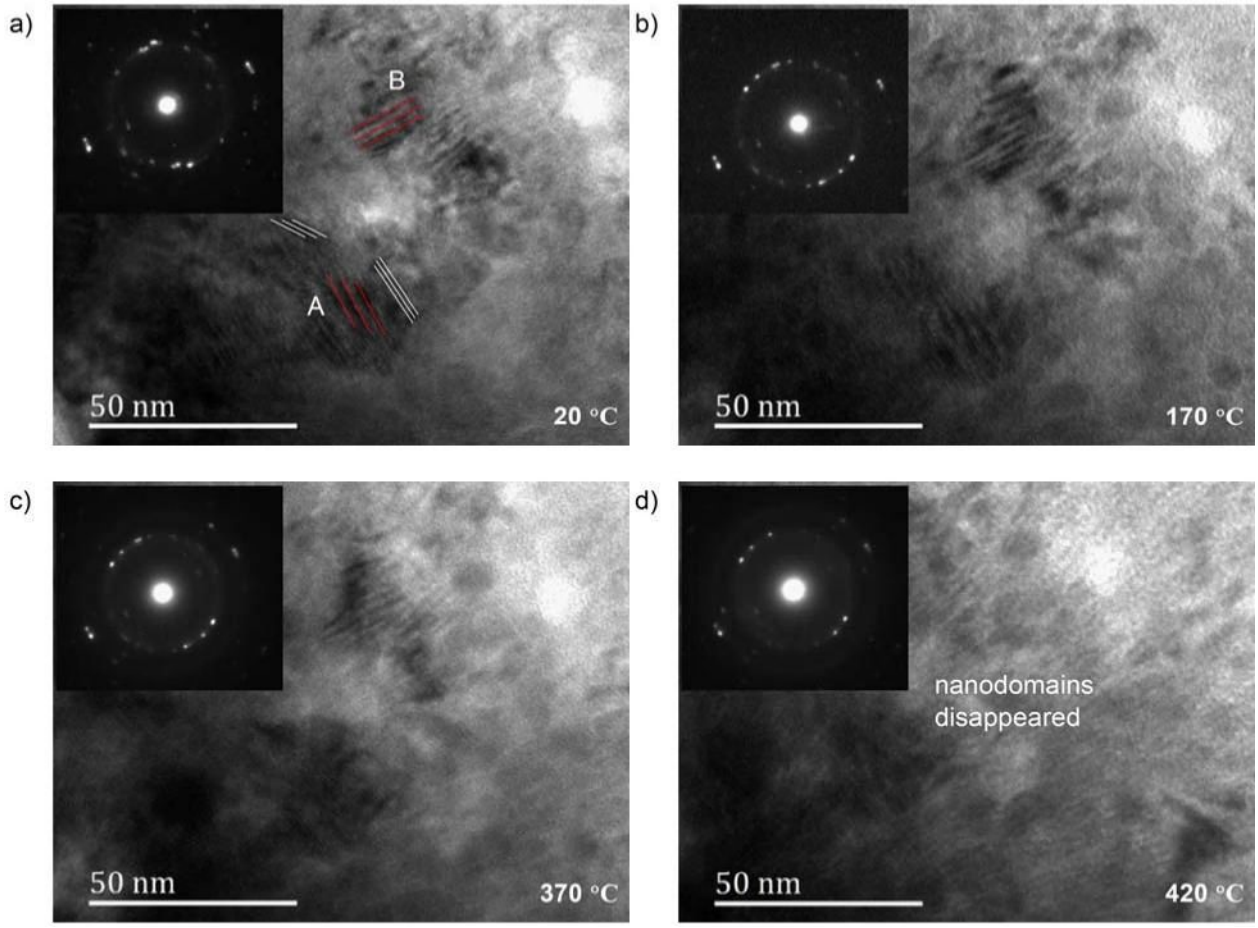

Figure 2. | Cross-sectional TEM images of the BCT-BMT thin film. (a) - (d) Evolution of ferroelectric nanodomains as the temperature increased from 20 °C to 470 °C.

Dielectric properties

Figure 3(a) shows the temperature dependence of dielectric permittivity ($e(T)$) and dielectric loss (tan $\hat{O}(T)$) of thin film. The peaks of dielectric permittivity are not obvious, and the $e(T)$ curves look highly flattened and dispersed. The dielectric permittivities around the peaks were fitted by a Lorentz-type empirical relation, $e_A/e=1+(T-T_A)^2/_2(\hat{O}_A)^2$,[23] where T_A ($T_A \neq T_c$) and e_A are the temperature of the dielectric permittivity peak and the extrapolated value of e at $T = T_A$, respectively. The fitted parameters $\hat{O}_A$ at 1, 10 and 100 kHz are 105.0, 106.4 and 121.9, respectively. They all are larger than that (103.6) of the prototypical relaxor $Pb(Mg_{1/3}Nb_{2/3})O_3$ ceramics, indicating a higher degree of relaxor dispersion.[23, 24] The extrapolated dielectric permittivities decrease sharply and greatly deviate from the experimental data with increasing temperature, as plotted by the

colored solid lines. However, the variation of the values of experimental data at 1 kHz was within ± 1% over a wide temperature range of 240 K (from 150 °C to 390 °C), indicating strong thermal insensitivity of dielectric permittivities (TIDP). The thermal insensitivity of dielectric permittivities was also investigated at 100 kHz. At this frequency, the tan δ remained less than 0.025 from 250 °C to 390 °C, and the variation of the resulting ε was also within ± 1%, indicating that the losses were not the dominant factor for the TIDP. Interestingly, the TIDP and the lamellar domains (see **Fig. 2(a) - 2(d)** and **Fig. S5(c) – S5(h)**) almost disappear together at the same temperature. Therefore, it can be inferred that the strong TIDP may be related to the behavior of lamellar nanodomains.

To gain further insight into the TIDP, the temperature dependence of the Raman scattering spectra of thin film was investigated (**Fig. 3(b)**). Neither did any new band appear, nor did any old band disappear, indicating that a relatively stable phase structure. To reveal the possible variation of each Raman mode with increasing temperature, the Raman spectra were well fitted by using eight characteristic peaks. The peaks 1 to 8, except peak 2, correspond to the $A_1(LO_3)/E(LO_4)$, $A_1TO_3/E(TO)$, $E(TO_3+LO)/B_1$, $A_1(TO_2)$, $A_1(TO_1)$, $E(TO_1)$, and $E(TO_2)$ modes, respectively.[25-27] The peak 2 (~ 605 - 609 cm^{-1}) is a new mode which only appears in the Raman spectra of Ba-based relaxor ferroelectric ceramics under high-pressure.[28] The peak 1 (~ 754 - 759 cm^{-1}) is attributed to the vibrations of polar $[(Ti/Mg)O_6]$ clusters, and its appearance is often regarded as a relaxor-characteristic signature. The peak 3 (~ 501 - 508 cm^{-1}) is due to the vibrations of the O-Ti/Mg-O symmetric stretching in tetragonally distorted polar $[(Ti/Mg)O_6]$ octahedral clusters. The peaks 4 (~ 311 - 325 cm^{-1}) is ascribed to the vibrations of asymmetric (Ti/Mg)-O phonon in tetragonal/orthorhombic phases. The peaks 5 (~ 212 - 223 cm^{-1}) is not only ascribed to the vibrations of asymmetric (Ti/Mg)-O phonon in tetragonal/orthorhombic phases but also in rhombohedral phase. The peaks 6 (~ 144 - 146 cm^{-1}), 7 (~ 96 - 97 cm^{-1}) and 8 (~ 68 - 69 cm^{-1}) are due to the vibrations of A-site atoms in perovskite structure.[29] Especially, the appearance of the peak 6 also indicates the existence of a local rhombohedral structure in the BCT-BMT thin film.[25, 30] However, the peak 6 (namely the $A_1(TO_1)$ mode) is Raman inactive in its bulk ceramics, as shown in

Fig. S6, indicating the absence of rhombohedral phase. Compared with the thin film, the A_{1g} mode looks more active in its bulk ceramics, indicating that some of Ca resides on the B-site rather than A-site.[31]

The variations of the peak position, the full width at half maxima (FWHM) and the integrated intensity of each characteristic peak are summarized in **Fig. 3(c)**, **3(d)** and **Fig. S7**. All peaks except the peak 8 in **Fig. 3(b)** almost linearly shift toward lower frequency regions with increasing temperature. The amounts of red-shift referred to room temperature for peaks 1, 2, 3, 4, 5, 6 and 7 at 300 °C were 4.5, 3.4, 5.6, 12.9, 9.4, 1.9 and 0.32 cm^{-1}, respectively. A weak blue-shift of 0.29 cm^{-1} was exerted to the peak 8. Similar to the variation of the peak position, the FWHMs of all peaks except peak 3 also change linearly with increasing temperature. Compared with the FWHM at room temperature, the variations of the FWHM for peak 1, 2, 4 and 5 at 300 °C are 9.9, 1.5, 19 and -11 cm^{-1}, respectively. The variations of the FWHM for peaks 6, 7 and 8 at 300 °C were almost negligible. Different to the linear variations of the FWHMs of peaks 4, 5 and 6, the FWHM of peak 3 oscillates slightly with a small amplitude (less than 4.5 cm^{-1}) with increasing temperature. The integrated intensity of peak 3 also follows a similar variation trend with increasing temperature, as shown in the **Fig. S7(l).** These results indicate that the distorted polar nanoclusters in thin film may be in a dynamic and thermally stable state by interacting with each other with increasing temperature, especially for the tetragonal phase. They will bring benefit to the high thermal stability of lamellar nandomains, and finally resulting in the strong TIDP.

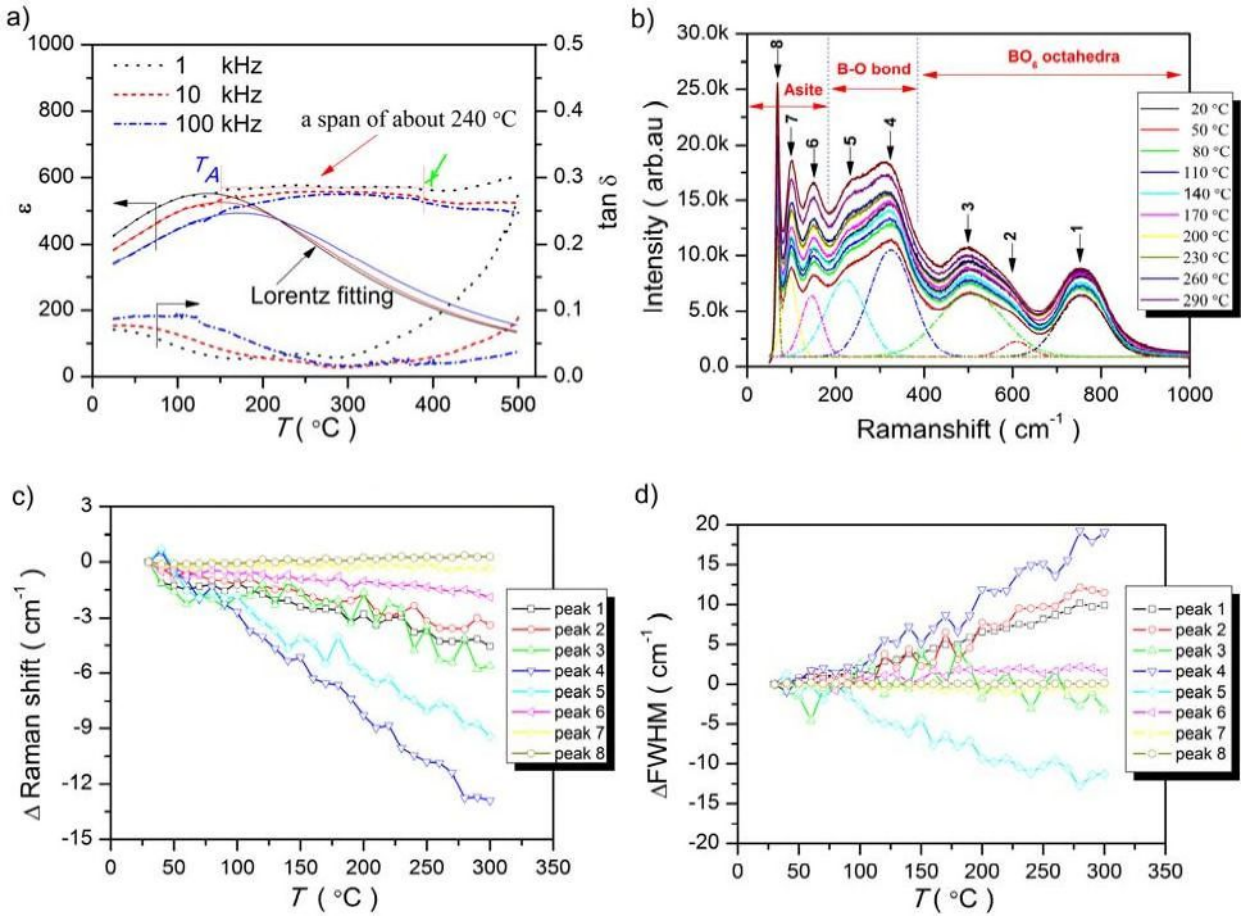

Figure 3. | $\varepsilon(T)$, tan $\delta(T)$ and Raman scattering spectra of the BCT-BMT thin film. (a) $\varepsilon(T)$ and tan $\delta(T)$. **(b)** Raman scattering spectra at selected temperatures. Changes of Raman shift **(c)** and FWHM **(d)** as a function of temperature of peaks 1-8. Peak 1 : $A_1(LO_3)/E(LO_4)$ mode (~754 - 759 cm^{-1}), Peak 2 : unknown mode (~ 605 - 609 cm^{-1}), Peak 3 : $A_1TO_3/E(TO)$ mode (~ 501 - 508 cm^{-1}), Peak 4 : $E(TO_3+LO)/B_1$ mode (~ 311 - 325 cm^{-1}), Peak 5 : $A_1(TO_2)$ mode (~ 212 - 223 cm^{-1}), Peak 6 : $A_1(TO_1)$ mode (~ 144 - 146 cm^{-1}), Peak 7 : $E(TO_1)$ mode (~ 96 - 97 cm^{-1}), Peak 8 : $E(TO_2)$ mode (~ 68 - 69 cm^{-1}).

Negative electrocaloric effect

Figure S8 shows the *P-E* loops and corresponding *I-E* curves of the BCT-BMT thin film at selected applied electric fields and frequencies (10 kHz and 10 Hz). With the increasing frequency and the applied electric field, the double-like *P-E* loops with four *I-E* peaks gradually degenerated into single *P-E* loops with two *I-E* peaks. According to previous research work, the double-like *P-E* loops at a lower electric field and frequency (see **Fig. S8a** and **Fig. S8c**) could be ascribed to the pinning and depinning of the domain walls by defects such as

bismuth vacancies and oxygen vacancies.[19] To avoid the interference and impact of defect dipoles on the evaluation of the *EC* effect of thin film,[17] the *P-E* loops at 10 kHz were adopted and collected at a step of ten degrees in the temperature range between 20 and 170 °C. The value of applied electric field plays an important role in obtaining a large ΔT [32, 33]: here a conservative electric field, well below the mean dielectric strength (DBS) estimated by the Weilbull distribution,[34, 35] **Fig. S9** was applied to avoid electrical breakdown.

To avoid dielectric breakdown, a safety electric field playing an important role in obtaining a large ΔT is applied,[32, 33] which is well below the mean dielectric strength (DBS) estimated by the Weilbull distribution,[34, 35] as shown in **Fig. S9**. The DBSs obtained at 10 kHz, 1k Hz, 100 Hz and 10 Hz are 2991 kV/cm, 2981 kV/cm, 2677 kV/cm and 2041 kV/cm, respectively, which are all much higher than 1798 kV/cm (the safety electric field applied in **Fig.S10**). Representative plots of *P-E* loops are shown in **Fig. S10**, respectively. The shape of *P-E* loops always keeps slim in the whole temperature range studied, indicating that the leakage current is low (**Fig. S11**) and the corresponding Joule heating is negligible to the ΔT. The temperature dependence of the polarization ($P(T)$) at selected electric fields was extracted from the upper branches of the *P-E* loops in $E > 0$ and presented in the lower right inset of **Fig. S10**, where the red solid lines represent cubic-spline interpolations of the raw experimental data. The temperature dependence of pyroelectric coefficients ($(\partial P/\partial T)_E(T)$) at selected electric fields was derived from the $P(T)$ curves and plotted in **Fig. S12**.

Based on the Maxwell relationship $(\partial S / \partial E)_T = (\partial P / \partial T)_E$, reversible adiabatic changes in temperature (ΔT) and entropy (ΔS) of dielectric materials can be indirectly estimated by:[2, 5, 6]

$$\Delta T = -\frac{1}{\rho}\int_{E_1}^{E_2}\frac{T}{C}\left(\frac{\partial P}{\partial T}\right)_E dE \qquad (1)$$

$$\Delta S_{entropy} = -\frac{1}{\rho}\int_{E_1}^{E_2}\left(\frac{\partial P}{\partial T}\right)_E dE \qquad (2)$$

where T is the temperature, P the maximum polarization at the applied electric field E, ρ the density, C the heat capacity, and $E1$ and $E2$ the initial and final applied electric field, respectively. The ρ and C in the

temperature range studied are 5.7 gcm^{-3} and 0.3 $JK^{-1}g^{-1}$, respectively. Some may question the validity of the applicability of **Eq. (1)** and **Eq. (2)** to a relaxor. As presented by Smolensky for relaxor ferroelectrics,[36] a statistical model is adopted in this work to illustrate the permittivity and temperature relationship because the nanoscale domains are distributed throughout the polycrystalline unit, resulting in compositional fluctuation, which leads the polarization versus temperature response to be similar but slightly different to that of a second-order phase transition. Thus, the Maxwell relation sometimes can be approximately used for relaxor ferroelectrics.[37] According to **Eq. (1)** and **Eq. (2)**, the adiabatic temperature change ΔT and entropy change ΔS of thin films are obtained and plotted against temperature T in **Fig. 4(a)** and its inset. Negative ΔT and ΔS peaks are observed. They shift significantly toward lower temperatures with increasing electric field from 247 to 1798 kV/cm as guided by the colored arrows, similar to those reported in antiferroelectric thin films and ceramics.[10, 11, 13] However, the ΔT and ΔS peaks in positive effect shift to higher temperatures with increasing electric field, as reported by previous experimental and theoretical works.[38, 39] The maximum ΔT which is near the right part of the Lorentz extrapolated peak (T_A) (see **Fig. 3(a)**) of dielectric permittivity is about – 42.5 K at ~ 163 °C and at 1632 $kVcm^{-1}$, and the corresponding ΔS is about – 29.3 $JK^{-1}kg^{-1}$. According to the Dulong-Peti law limit,[40] for perovskite relaxor ferroelectric thin films, the permitted ultimate upper bound of $_{\Delta Tmax}$ is about – 60 K at this temperature. Therefore, the giant ΔT ~ – 42.5 K of BCT-BMT thin film can be acceptable. As far as we know, the giant negative EC effect obtained in this work is the best result among pure perovskite materials reported to date. Although the maximum ΔT ~ -52.2 K was obtained at low temperature (182 K) in the $PbZr_{0.53}TiO_{0.47}/CoFe_2O_4$ ferroelectric/ferromagnetic multilayered thin films due to the magneto-electric coupling,[18] the negative EC effect reduced sharply at higher working temperatures (e.g., 230 K), due to the weaker magneto-electric coupling.

The mechanism underlying the negative EC effect in relaxors and AFEs is still elusive. Nevertheless, the entropy change stimulated by the change of electric field-induced ordering or disordering states of dipoles is the widely accepted phenomenological physical explanation. To understand the origin of the negative EC effect in relaxors and AFEs, some theoretical insightful models based on the first-principles have been developed, such as the subtle coupling between AFE, FE and oxygen tilting instabilities, defect dipoles, and

so on.[10, 13-17] However, these models could not provide a comprehensive solution to the giant negative EC effect in this study.

To get insight into the giant negative EC effect in the BCT-BMT lead-free thin film, the dc bias electric field dependence of Raman scattering spectra was investigated (**Fig. S13 and Fig. S14**). The Agilent 4294A was used as the dc bias source, it also acted as a monitor to alert if the voltage applied to the thin film was close to electrical breakdown, in order to ensure reliable experimental data. A highly conductive and transparent ITO thin film with ~ 1 mm diameter was used as the top electrode, as shown in the inset of **Fig. 4(b)** which shows the Raman scattering spectra at selected dc bias electric fields. The Raman scattering spectra at each selected dc bias electric field was well fitted by using a multi-peak fitting method. The variation of the peak position, the FWHM and the integrated intensity of each characteristic peak were summarized in **Fig. S15** and **Fig. 4(c)**. All peaks except peak 2 shifted toward lower frequencies with the increase of dc bias electric field. Meanwhile, the corresponding FWHM increased with increasing electric field except that of peak 1. The increased FWHM of peak 3 is the biggest one among all peaks, indicating an increased anharmonicity of the O-Ti/Mg-O symmetric stretching vibrations in tetragonally distorted polar [$(Ti/Mg)O_6$] octahedral clusters. As a result, the degree of disorder for the tetragonal phase in the BCT-BMT thin film was enhanced with increased dc bias electric field.[41] Physically, the greater the disorder increase, the larger the entropy increase. Accordingly, a negative *EC* effect could be induced. Therefore, it is inferred that the giant negative *EC* effect in the BCT-BMT thin film may be related to the phase transition induced by electric field, especially for the tetragonal phase. In order to further reveal the phase transition induced by an electric field, the dc bias electric field dependence of XRD patterns was also investigated (**Fig. S16**). As shown in the inset of **Fig. 4(c)**, when the dc bias electric field increased from 0 kV/cm to 375 kV/cm, the split diffraction peaks around 31.5 °2θ had merged into one peak, indicating an electric-field induced structural phase transition (nanoscale tetragonal & orthorhombic to rhombohedral).

The electric field induced structural phase transition in the (111)-oriented BCT-BMT lead-free thin film can also be confirmed by thermodynamic method. According to previous research work, the

quadratic in polarization terms of the thermodynamic potential,[42, 43] which control the polarization response, can be rewritten as:

$$\Delta G = \frac{T - T_0 - A_{\text{in}} u_{\text{m}}}{2\varepsilon_0 C}(P_1^2 + P_2^2) + \frac{T - T_0 - A_{\text{out}} u_{\text{m}}}{2\varepsilon_0 C} P_3^2 + \text{high order} \quad (3)$$

Where, for (001)-oriented films,

$$A_{in} = 2\varepsilon_0 C \frac{Q_{11} + Q_{12}}{s_{11} + s_{12}} \quad (4)$$

$$A_{out} = 2\varepsilon_0 C \frac{2Q_{12}}{s_{11} + s_{12}} \quad (5)$$

And, for (111)-oriented films,

$$A_{in} = 2\varepsilon_0 C \frac{4(Q_{11} + 2Q_{12} + Q_{44}/2)}{4s_{11} + 8s_{12} + s_{44}} \quad (6)$$

$$A_{out} = 2\varepsilon_0 C \frac{4(Q_{11} + 2Q_{12} - Q_{44})}{4s_{11} + 8s_{12} + s_{44}} \quad (7)$$

where P_1 and P_2 stand for two in-plane components of the polarization while P_3 the out-of-plane component of the polarization, respectively. The ε_0 is the permittivity of free space, T_0 the Curie-Weiss temperature and C the Curie-Weiss constant. Q_{11}, Q_{12}, and Q_{44} are the relevant cubic electrostrictive coefficient and S_{11}, S_{12} and S_{44} are the cubic elastic compliances at constant dielectric displacements. The values of parameters A_{in} and A_{out} for some perovskite ferroelectrics are listed in **Table** [S1,42-44] The parameters given in **Table S1** clearly suggest that the polarization response of the strained films is anisotropic. Obviously, (111)-oriented ferroelectric films have a weaker anisotropic property than (001)-oriented ferroelectric films. So the *R* phase can be more easily produced, especially by applying an electric field *E* in [111] direction.

As shown in **Fig. 4(d)**, when the electric field *E* is applied along the [111] direction, namely the out-of-plane of the BCT-BMT thin film, the *T* phase is transformed into the *R* phase, and the *O* phase is also induced into the *R* phase. Although the overall polarizations $(P_T[001]$ and $P_O[110])$ of *T* and *O* phases decrease as the temperature increases, the component polarizations $(P_T[111]$ and $P_O[111])$ in the [111] direction increase due to the electric field induced *T*-*R* and *O*-*R* phase transitions as confirmed by the results of Raman spectra and XRD pattern under the dc bias electric fields. During the two phase transitions, as the polarization direction changes, α' or β' will decrease with the increasing temperature, but cos (α') and cos (β') will increase, so the polarization ($P_{[111]}$) in the [111] direction will increase with the increasing temperature. As a result, the value of the

pyroelectric coefficient $(\partial P_{[111]}/\partial T)$ will be positive, as shown in the inset of **Fig. 4(d)**, leading to a negative *EC* effect in the (111)-oriented BCT-BMT lead-free thin film.

The giant negative *EC* effect of the BCT-BMT thin film shows the high feasibility of this material for next-generation chip-cooling applications, in addition to its other merits, such as its lead-free, inorganic, and highly Si-compatible nature compared to conventional Pb-based materials and organic ferroelectrics. Furthermore, the giant negative *EC* effect of the BCT-BMT thin film could in future be further improved by various strategies. Firstly, doping the thin film with other dopants, such as Sr and La which can lower and extend the working temperature, [2, 45] is an effective pathway to meet practical applications around room temperature. Secondly, increasing the thickness of thin film to micrometer scale by spin-coating can be easily realized by the sol-gel method. The sol-gel thin films with thickness in the micrometer range can increase the total cooling capacity by several orders of magnitude compared to thin films with thickness in the nanometer range. Moreover, the combination of positive and negative *EC* effects can complete the cooling process in one step with a sustained applied electric field in the cooling process, as suggested by Li et al.,[46] which might enable a more efficient refrigeration process. As a result, designing the solid-state refrigerators without any moving parts and without the need for the periodic application and withdrawal of an electric field by using lead-free film materials with giant positive and negative EC effects will be a highly attractive strategy for next-generation green chip cooling.[12, 46]

Moreover, a large recoverable energy density (W_{energy}) ~ 51.7 Jcm^{-3} at 2879 kVcm^{-1} (green shaded area in **Fig. 5(a))** can also be obtained in the lead-free BCT-BMT thin film. It is comparable to the best lead-containing thin films such as the PLZT (53 Jcm^{-3} at 3500 kVcm^{-1}) and also the best lead-free compounds such as the terpolymer nanocomposite with doped boron nitride nanosheets (20.3 Jcm^{-3} at 6500 kVcm-1),[47, 48] etc. As a thin film capacitor, the charging/discharging time is about 0.8 μs (**Fig. S17a** and **S17b**). Correspondingly, the power density is ~ 1.15×10^{10} Wkg^{-1}. As shown by the Ragone plot in **Figure 5b**, it can be found that high power density and large energy density (51.7 J cm^{-3} & 2.5 Whkg^{-1}) can be achieved simultaneously in the BCT-BMT thin film capacitor. These results indicate that the BCT-BMT thin film is also a very promising, environmentally friendly, low cost (compared with niobium-based and scandium-based materials),[49, 50] and thermally stable (compared with polymers) ceramic capacitor material for potential applications in electric energy storage.

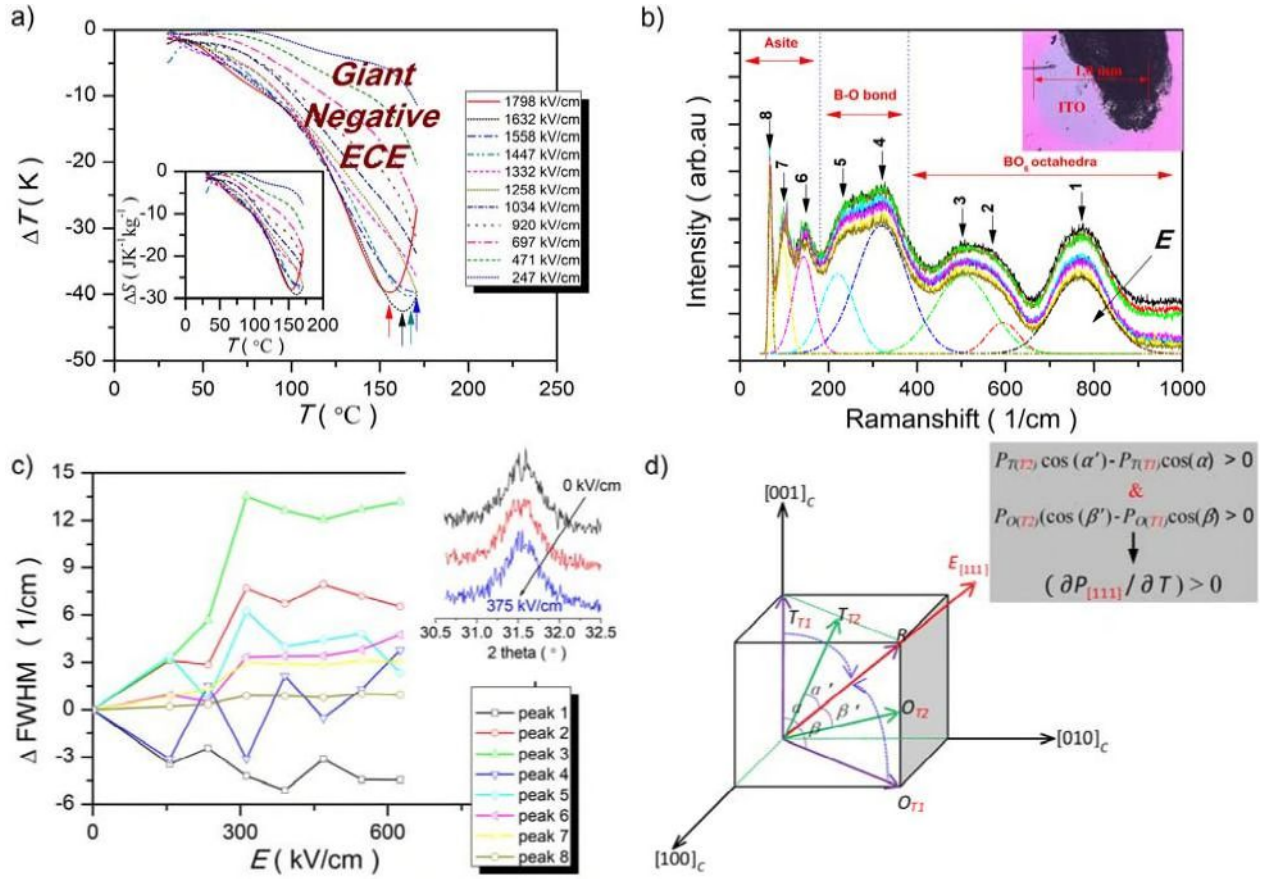

Figure 4. | Electrocaloric effect of the BCT-BMT thin films. (a) $\Delta T(T)$ at selected electric fields. Inset: $\Delta S(T)$. **(b)** Raman scattering spectra at selected electric fields. Inset: ITO top electrode bridged by silver paster. **(c)** Change of FWHM as a function of dc bias electric field. Inset: XRD patterns at dc electric fields. **(d)** Phase transition diagram of tetragonal/orthorhombic to rhombohedral under the electric field. Inset: positive pyroelectric coefficient along [111] direction.

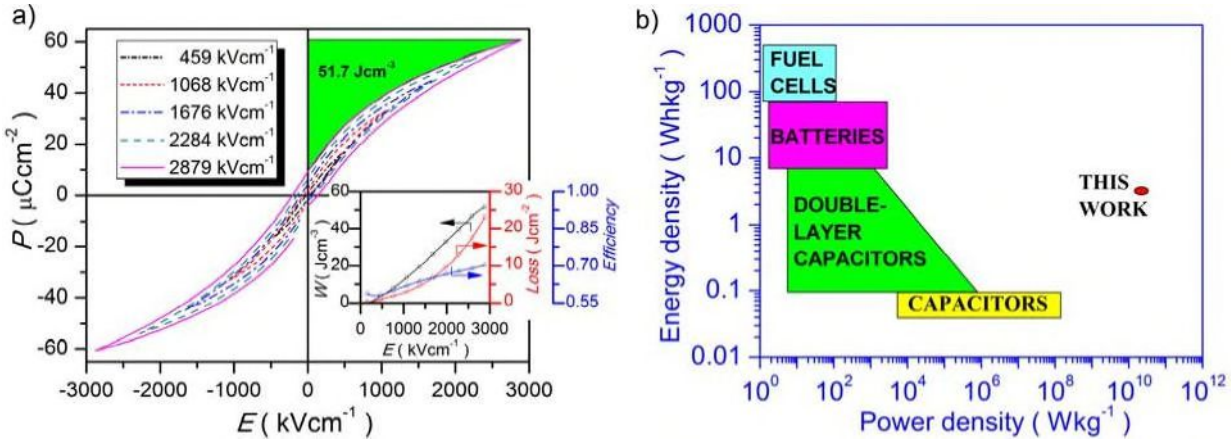

Figure 5. | Energy density and power density measurements of the BCT-BMT thin film. (a) *P-E* loops. Inset: W_{energy}, W_{loss}, and η versus *E*. **(b)** Energy density & power density diagram.

Conclusion

A giant negative *EC* effect with maximum $\Delta T \sim -42.5$ K and $\Delta S \sim -29.3$ J K^{-1} kg^{-1} which are comparable to the best reported positive *EC* effects so far was realized in BCT-BMT lead-free relaxor ferroelectric thin films. An out-of-plane electric-field induced structural phase transition (nanoscale tetragonal and orthorhombic to rhombohedral) is responsible for the giant negative *EC* effect. Meanwhile, a large energy density of 51.7 J cm^{-3} with a high power density of 1.15×10^{10} W kg^{-1} at room temperature is also achieved in the thin film. These breakthroughs indicate that the BCT-BMT thin film is not only a promising material for application in next-generation green chip refrigeration devices but also an attractive multifunctional material.

Methods:

Fabrication:

BCT-BMT thin films were grown by using a sol-gel method as shown in **Fig. S18.** $Bi(CH_3COO)_3$ with 20% excess Bi, $Ca(CH_3COO)_2$ and $Ba(CH_3COO)_2$ were dissolved in glacial acetic at 80 °C. Simultaneously, $Mg(OC_2CH_5)_2$ with 20% excess Mg and $Ti(OCH(CH_3)_2)_4$ were dissolved in a mixture of $CH_3OCH_2CH_2OH$ and $CH_3COCH_2COCH_3$. The Bi/Ca/Ba and Mg/Ti solutions were then mixed and stirred for 30 min at room temperature. The final concentration of the BCT-BMT precursor solution was 0.2 M. After aging of the

precursor solution for 24 h, the BCT-BMT thin film was deposited on Pt(111)/TiO_x/SiO_2/Si(100) substrate that were rinsed with acetone and ethanol prior to the deposition. Each layer of BCT-BMT film was spin-coated at 4000 rpm for 30 s. To eliminate the formation of cracks, every wet film was first dried at 150 °C for 3 min and then pyrolyzed at 450 °C for another 3 min on a hotplate. After the deposition of 8 layers, the film was annealed in a chamber furnace at 700 °C for 30 min in air. The final thickness of the film was about 320 nm, as determined by the cross-sectional micrographs.

Characterization:

The crystallinity of the BCT-BMT thin film was monitored by X-ray diffraction (XRD; Rigaku 9 KW Smartlab, Tokyo, Japan). The cross-sectional morphology of the film was examined by scanning electron microscopy (FEI Sirion 200). The microstructure of the film was studied by transmission electron microscopies (TEMs; Titan Cubed Themis G2300 and JEOL JEM-2100F). The out-of-plane feature of the film was investigated by scanning probe microscopies (Bruker Multimode 8 and Asylum Research MFP-3D). The Raman scattering spectra were acquired by a Raman spectrometer (Horiba HR800) with an excitation laser wavelength of 488 nm. For measurement of the electrical properties, square Au/Cr top electrodes with an edge length of 90 μm (inset of **Fig. S2**) were deposited by RF magnetron sputtering using a shadow mask. Dielectric permittivity measurement was carried out using an impedance analyzer (E4980A, Agilent) with a perturbation voltage Vac = 100 mV. Polarization-electric field (*P*-*E*) hysteresis loops and leakage currents were obtained by means of a ferroelectric tester (Precision Premier II, Radiant Technologies Inc., Alpharetta, GA). The charge/discharge experiment (**Fig. S17**) was carried out using a versatile signal source (81150A, Agilent) and a digital oscilloprobe (HDO4104, leCroy). The injected pulse voltage, duty cycle and the load impedance are set to 5 V, 50% and 50 Ω, respectively. Raman scattering spectra and XRD patterns as a function of dc bias electric field were investigated (**Fig. S13, S14, S15 and S16**) using the Agilent 4294A as the dc bias source. The ITO with high transparency and electro-conductivity was used as the top electrode with ~ 1mm diameter (**Fig. S14**). All samples were measured with top-to-bottom electrode configuration. The temperature of the sample was controlled by a thermal controller (THMSG600, Linkam) with an accuracy of 0.1 °C.

Acknowledgements

This work was supported by the Research Grants Council of the Hong Kong Special Administrative Region, China (Project No. PolyU152665/16E), the National Natural Science Foundation of China (51402196、51602159), the Guangxi Natural Science Foundation (Grants 2016GXNSFCB380006, 2017GXNSFFA198015), and the Scientific Research Foundation of Guangxi University (Grant XTZ160530).

Author Contributions

Biaolin Peng, Haitao Huang and Qi Zhang conceived the idea and designed the experiments. Biaolin Peng fabricated the samples and carried out most of the experiments. Biaolin Peng carried out the TEM work. Biaolin Peng and Gang Bai constructed the interpretation part of the T/O-R phase transition. Biaolin Peng, Qi Zhang, and Haitao Huang wrote the paper. All the authors participated in the analysis and discussion of the results.

Additional information

Competing financial interests: The authors declare no competing financial interests.

References

[1] X. Hao, J. Zhai, L. B. Kong, Z. Xu, A comprehensive review on the progress of lead zirconate-based antiferroelectric materials[J]. *Progress in Materials Science*, 2014, **63**: 1-57.

[2] B. Peng, Q. Zhang, Y. Lyu, L. Liu, X. Lou, C. Shaw, H. Huang, Z. Wang, Thermal strain induced large electrocaloric effect of relaxor thin film on $LaNiO_3$/Pt composite electrode with the coexistence of nanoscale antiferroelectric and ferroelectric phases in a broad temperature range[J]. *Nano Energy*, 2018, **47**: 285-293.

[3] X. Moya, S. Kar-Narayan, N. D. Mathur, Caloric materials near ferroic phase transitions[J]. *Nature Materials*, 2014, **13**(5): 439-450.

[4] A. S. Mischenko, Q. Zhang, J. F. Scott, R. W. Whatmore, N. D. Mathur, Giant electrocaloric effect in thin-film $PbZr_{0.95}Ti_{0.05}O_3$[J]. *Science*, 2006, **311**(5765): 1270-1271.

[5] B. Neese, B. J. Chu, S. G. Lu, Y. Wang, E. Furman, Q. M. Zhang, Large electrocaloric effect in ferroelectric polymers near room temperature[J]. *Science*, 2008, **321**(5890): 821-823.

[6] B. L. Peng, H. Q. Fan, Q. Zhang, A Giant Electrocaloric Effect in Nanoscale Antiferroelectric and Ferroelectric Phases Coexisting in a Relaxor $_{Pb0.8Ba0.2ZrO3}$ Thin Film at Room Temperature[J]. *Advanced Functional Materials*, 2013, 23(23): 2987-2992.

[7] Y. Zhao, X. H. Hao, Q. Zhang, A giant electrocaloric effect of a $_{Pb0.97La0.02(Zr0.75Sn0.18Ti0.07)O3}$ antiferroelectric thick film at room temperature[J]. *Journal of Materials Chemistry C*, 2015, 3(8): 1694-1699.

[8] T. M. Correia, S. Kar-Narayan, J. S. Young, J. F. Scott, N. D. Mathur, R. W. Whatmore, Q. Zhang, PST thin films for electrocaloric coolers[J]. *Journal of Physics D-Applied Physics*, 2011, 44(16):

[9] H. Gu, X. Qian, X. Li, B. Craven, W. Zhu, A. Cheng, S. C. Yao, Q. M. Zhang, A chip scale electrocaloric effect based cooling device[J]. *Applied Physics Letters*, 2013, 102(12): 122904.

[10] W. Geng, Y. Liu, X. Meng, L. Bellaiche, J. F. Scott, B. Dkhil, A. Jiang, Giant Negative Electrocaloric Effect in Antiferroelectric La-Doped Pb(ZrTi)O_3 Thin Films Near Room Temperature[J]. *Adv Mater*, 2015, 27(20): 3165-9.

[11] M. Ye, T. Li, Q. Sun, Z. Liu, B. Peng, C. Huang, P. Lin, S. Ke, X. Zeng, X. Peng, L. Chen, H. Huang, A giant negative electrocaloric effect in Eu-doped $PbZrO_3$ thin films[J]. *Journal of Materials Chemistry C*, 2016, 4(16): 3375-3378.

[12] M. H. Park, H. J. Kim, Y. J. Kim, T. Moon, K. Do Kim, Y. H. Lee, S. D. Hyun, C. S. Hwang, Giant Negative Electrocaloric Effects of $_{Hf0.5Zr0.5O2}$ Thin Films[J]. *Advanced Materials*, 2016, 28(36): 7956-7961.

[13] R. Pirc, B. Rožič, J. Koruza, B. Malič, Z. Kutnjak, Negative electrocaloric effect in antiferroelectric $PbZrO_3$[J]. *Europhysics Letters*, 2014, 107(1): 17002.

[14] A. R. Akbarzadeh, S. Prosandeev, E. J. Walter, A. Al-Barakaty, L. Bellaiche, Finite-temperature properties of Ba(Zr,Ti)O_3 relaxors from first principles[J]. *Phys Rev Lett*, 2012, 108(25): 257601.

[15] J. Íñiguez, M. Stengel, S. Prosandeev, L. Bellaiche, First-principles study of the multimode antiferroelectric transition in$PbZrO_3$[J]. *Physical Review B*, 2014, 90(22):

[16] I. Ponomareva, S. Lisenkov, Bridging the Macroscopic and Atomistic Descriptions of the Electrocaloric Effect[J]. *Physical Review Letters*, 2012, 108(16):

[17] Y.-B. Ma, A. Grünebohm, K.-C. Meyer, K. Albe, B.-X. Xu, Positive and negative electrocaloric effect in $BaTiO_3$ in the presence of defect dipoles[J]. *Physical Review B*, 2016, 94(9):

[18] G. Vats, A. Kumar, N. Ortega, C. R. Bowen, R. S. Katiyar, Giant pyroelectric energy harvesting and a negative electrocaloric effect in multilayered nanostructures[J]. *Energy & Environmental Science*, 2016, 9(4): 1335-1345.

[19] S. Wada, K. Yamato, P. Pulpan, N. Kumada, B.-Y. Lee, T. Iijima, C. Moriyoshi, Y. Kuroiwa, Piezoelectric properties of high Curie temperature barium titanate–bismuth perovskite-type oxide system ceramics[J]. *Journal of Applied Physics*, 2010, 108(9): 094114.

[20] A. Zeb, S. J. Milne, S. Zhang, Stability of High-Temperature Dielectric Properties for $(1 - x)Ba_{0.8}Ca_{0.2}TiO_3$-$xBi(Mg_{0.5}Ti_{0.5})O_3$ Ceramics[J]. *Journal of the American Ceramic Society*, 2013, 96(9): 2887-2892.

[21] W. Qu, X. Tan, Texture control and ferroelectric properties of $Pb(Nb,Zr,Sn,Ti)O_3$ thin films prepared by chemical solution method[J]. *Thin Solid Films*, 2006, 496(2): 383-388.

[22] A. K. Tagantsev, N. A. Pertsev, P. Muralt, N. Setter, Strain-induced diffuse dielectric anomaly and critical point in perovskite ferroelectric thin films[J]. *Physical Review B*, 2001, 65(1):

[23] S. Ke, H. Fan, H. Huang, H. L. W. Chan, Lorentz-type relationship of the temperature dependent dielectric permittivity in ferroelectrics with diffuse phase transition[J]. *Applied Physics Letters*, 2008, 93(11):

[24] B. Peng, Q. Zhang, X. Li, T. Sun, H. Fan, S. Ke, M. Ye, Y. Wang, W. Lu, H. Niu, J. F. Scott, X. Zeng, H. Huang, Giant Electric Energy Density in Epitaxial Lead-Free Thin Films with Coexistence of Ferroelectrics and Antiferroelectrics[J]. *Advanced Electronic Materials*, 2015, 1(5):

[25] M. B. Abdessalem, S. Aydi, A. Aydi, N. Abdelmoula, Z. Sassi, H. Khemakhem, Polymorphic phase transition and morphotropic phase boundary in $_{Ba1-xCaxTi1-yZryO3}$ ceramics[J]. *Applied Physics A*, 2017, 123(9):

[26] V. S. Puli, A. Kumar, D. B. Chrisey, M. Tomozawa, J. F. Scott, R. S. Katiyar, Barium zirconate-titanate/barium calcium-titanate ceramics via sol-gel process: novel high-energy-density capacitors[J]. *Journal of Physics D-Applied Physics*, 2011, 44(39): 395403.

[27] M. W. Chu, Y. Shingaya, T. Nakayama, Effect of 90 deg ferroelastic twin walls on lattice dynamics of nanocrystalline tetragonal ferroelectric perovskites[J]. *Applied Physics A*, 2006, 86(1): 101-106.

[28] J. Kreisel, P. Bouvier, M. Maglione, B. Dkhil, A. Simon, High-pressure Raman investigation of the Pb-free relaxor $BaTi_{0.65}Zr_{0.35}O_3$[J]. *Physical Review B*, 2004, 69(9): 092104.

[29] A. Chaves, R. S. Katiyar, S. P. S. Porto, Coupled modes with A_1 symmetry in tetragonal $BaTiO_3$[J]. *Physical Review B*, 1974, 10(8): 3522.

[30] P. S. Dobal, R. S. Katiyar, Studies on ferroelectric perovskites and Bi-layered compounds using micro-Raman spectroscopy[J]. *Journal of Raman Spectroscopy*, 2002, 33(6): 405-423.

[31] V. S. Puli, A. Kumar, D. B. Chrisey, M. Tomozawa, J. F. Scott, R. S. Katiyar, Barium zirconate-titanate/barium calcium-titanate ceramics via sol–gel process: novel high-energy-density capacitors[J]. *Journal of Physics D: Applied Physics*, 2011, 44(39): 395403.

[32] S. G. Lu, Z. H. Cai, Y. X. Ouyang, Y. M. Deng, S. J. Zhang, Q. M. Zhang, Electrical field dependence of electrocaloric effect in relaxor ferroelectrics[J]. *Ceramics International*, 2015, 41: S15-S18.

[33] S. G. Lu, B. Rozic, Q. M. Zhang, Z. Kutnjak, R. Pirc, Electrocaloric effect in ferroelectric polymers[J]. *Applied Physics a-Materials Science & Processing*, 2012, 107(3): 559-566.

[34] Y. Zhao, X. Hao, M. Li, Dielectric properties and energy-storage performance of $_{(Na0.5Bi0.5)TiO3}$ thick films[J]. *Journal of Alloys and Compounds*, 2014, 601: 112-115.

[35] L. Zhang, X. Hao, Dielectric properties and energy-storage performances of $_{(1-x)(Na0.5Bi0.5)TiO3–xSrTiO3}$ thick films prepared by screen printing technique[J]. *Journal of Alloys and Compounds*, 2014, 586(0): 674-678.

[36] G. A. e. Smolenskii, Physical phenomena in ferroelectrics with diffused phase transition[J]. *J. Phys. Soc. Jpn*, 1970, 28(1): 26-37.

[37] X. D. Jian, B. Lu, D. D. Li, Y. B. Yao, T. Tao, B. Liang, J. H. Guo, Y. J. Zeng, J. L. Chen, S. G. Lu, Direct Measurement of Large Electrocaloric Effect in $_{Ba(ZrxTi1-x)O3}$ Ceramics[J]. *ACS Appl Mater Interfaces*, 2018, 10(5): 4801-4807.

[38] B. Peng, Q. Zhang, X. Li, T. Sun, S. Ke, M. Ye, Y. Wang, W. Lu, H. Niu, X. Zeng, H. Fan, H. Huang, High dielectric tunability, electrostriction strain and electrocaloric strength at a tricritical point of tetragonal, rhombohedral and pseudocubic phases[J]. *Journal of Alloys and Compounds*, 2015, 646: 597-602.

[39] M. C. Rose, R. E. Cohen, Giant Electrocaloric Effect Around T_c[J]. *Physical Review Letters*, 2012, 109(18): 187604.

[40] R. Pirc, Z. Kutnjak, R. Blinc, Q. M. Zhang, Upper bounds on the electrocaloric effect in polar solids[J]. *Applied Physics Letters*, 2011, 98(2):

[41] X. Chen, Z. G. Hu, Z. H. Duan, X. F. Chen, G. S. Wang, X. L. Dong, J. H. Chu, Effects from A-site substitution on morphotropic phase boundary and phonon modes of $_{(Pb1–1.5xLax)(Zr0.42Sn0.40Ti0.18)O3}$ ceramics by temperature dependent Raman spectroscopy[J]. *Journal of Applied Physics*, 2013, 114(4): 043507.

[42] N. A. Pertsev, A. G. Zembilgotov, A. K. Tagantsev, Effect of mechanical boundary conditions on phase diagrams of epitaxial ferroelectric thin films[J]. *Physical Review Letters*, 1998, 80(9): 1988-1991.

[43] M. Mtebwa, A. K. Tagantsev, T. Yamada, P. Gemeiner, B. Dkhil, N. Setter, Single-domain (110)$PbTiO_3$ thin films: Thermodynamic theory and experiments[J]. *Physical Review B*, 2016, 93(14):

[44] H. Zhang, X. Lu, R. Wang, C. Wang, L. Zheng, Z. Liu, C. Yang, R. Zhang, B. Yang, W. Cao, Phase coexistence and Landau expansion parameters for a $0.70Pb(Mg_{1/3}Nb_{2/3})O_3-0.30PbTiO_3$ single crystal[J]. *Physical Review B*, 2017, 96(5):

[45] J. A. Rodriguez, A. Etxeberria, L. Gonzalez, A. Maiti, Structural and electronic properties of $PbTiO_3$, $PbZrO_3$, and $PbZr_{0.5}Ti_{0.5}O_3$: First-principles density-functional studies[J]. *Journal of Chemical Physics*, 2002, 117(6): 2699-2709.

[46] B. Li, J. B. Wang, X. L. Zhong, F. Wang, Y. K. Zeng, Y. C. Zhou, The coexistence of the negative and positive electrocaloric effect in ferroelectric thin films for solid-state refrigeration[J]. *EPL (Europhysics Letters)*, 2013, 102(4): 47004.

[47] Q. Li, G. Zhang, F. Liu, K. Han, M. R. Gadinski, C. Xiong, Q. Wang, Solution-processed ferroelectric terpolymer nanocomposites with high breakdown strength and energy density utilizing boron nitride nanosheets[J]. *Energy & Environmental Science*, 2015, 8(3): 922-931.

[48] B. Ma, D.-K. Kwon, M. Narayanan, U. Balachandran, Dielectric properties and energy storage capability of antiferroelectric $Pb_{0.92}La_{0.08}Zr_{0.95}Ti_{0.05}O_3$ film-on-foil capacitors[J]. *Journal of Materials Research*, 2011, 24(09): 2993-2996.

[49] H. Ogihara, C. A. Randall, S. Trolier-McKinstry, High-Energy Density Capacitors Utilizing $0.7BaTiO_3$-$0.3BiScO_3$ Ceramics[J]. *Journal of the American Ceramic Society*, 2009, 92(8): 1719-1724.

[50] K. Yao, S. Chen, M. Rahimabady, M. S. Mirshekarloo, S. Yu, F. E. H. Tay, T. Sritharan, L. Lu, Nonlinear Dielectric Thin Films for High-Power Electric Storage With Energy Density Comparable With Electrochemical Supercapacitors[J]. *Ieee Transactions on Ultrasonics Ferroelectrics and Frequency Control*, 2011, 58(9): 1968-1974.

2019-05-02

Phase-transition induced giant negative electrocaloric effect in a lead-free relaxor ferroelectric thin film

Peng, Biaolin

Royal Society of Chemistry

Peng B, Zhang Q, Gang B, et al., (2019) Phase-transition induced giant negative electrocaloric effect in a lead-free relaxor ferroelectric thin film. Energy and Environmental Science, Volume 12, Issue 5, May 2019, pp. 1708-1717

https://doi.org/10.1039/c9ee00269c